Mechanism of Gold-Assisted Exfoliation of Centimeter-Sized Transition-Metal Dichalcogenide Monolayers

Velický, M., Donnelly, G. E., Hendren, W. R., McFarland, S., Scullion, D., DeBenedetti, W. J. I., Correa, G. C., Han, Y., Wain, A. J., Hines, M. A., Muller, D. A., Novoselov, K. S., Abruña, H. D., Bowman, R. M., Santos, E. J. G., & Huang, F. (2018). Mechanism of Gold-Assisted Exfoliation of Centimeter-Sized Transition-Metal Dichalcogenide Monolayers. *ACS Nano*, *12*(10), 10463-10472. https://doi.org/10.1021/acsnano.8b06101

Published in:
ACS Nano

Document Version:
Publisher's PDF, also known as Version of record

Queen's University Belfast - Research Portal:
Link to publication record in Queen's University Belfast Research Portal

Publisher rights
Copyright 2018 the authors.
This is an open access article published under a Creative Commons Attribution License (https://creativecommons.org/licenses/by/4.0/), which permits unrestricted use, distribution and reproduction in any medium, provided the author and source are cited.

General rights
Copyright for the publications made accessible via the Queen's University Belfast Research Portal is retained by the author(s) and / or other copyright owners and it is a condition of accessing these publications that users recognise and abide by the legal requirements associated with these rights.

Take down policy
The Research Portal is Queen's institutional repository that provides access to Queen's research output. Every effort has been made to ensure that content in the Research Portal does not infringe any person's rights, or applicable UK laws. If you discover content in the Research Portal that you believe breaches copyright or violates any law, please contact openaccess@qub.ac.uk.

Download date:27. Aug. 2022

This is an open access article published under a Creative Commons Attribution (CC-BY) License, which permits unrestricted use, distribution and reproduction in any medium, provided the author and source are cited.

ACS NANO

Cite This: ACS Nano 2018, 12, 10463−10472

www.acsnano.org

ARTICLE

Mechanism of Gold-Assisted Exfoliation of Centimeter-Sized Transition-Metal Dichalcogenide Monolayers

Matěj Velický,*[,†,‡,§] Gavin E. Donnelly,[†] William R. Hendren,[†] Stephen McFarland,[†] Declan Scullion,[†] William J. I. DeBenedetti,[§] Gabriela Calinao Correa,[∥] Yimo Han,[⊥] Andrew J. Wain,[#] Melissa A. Hines,[§] David A. Muller,[⊥,▽] Kostya S. Novoselov,[‡] Héctor D. Abruña,[§] Robert M. Bowman,[†] Elton J. G. Santos,[†] and Fumin Huang*[,†]

[†]School of Mathematics and Physics, Queen's University Belfast, University Road, Belfast BT7 1NN, United Kingdom

[‡]School of Physics and Astronomy, University of Manchester, Oxford Road, Manchester M13 9PL, United Kingdom

[§]Department of Chemistry and Chemical Biology, Cornell University, Ithaca, New York 14853, United States

[∥]Department of Material Science and Engineering, Cornell University, Ithaca, New York 14853, United States

[⊥]School of Applied and Engineering Physics, Cornell University, Ithaca, New York 14853, United States

[#]National Physical Laboratory, Teddington TW11 0LW, United Kingdom

[▽]Kavli Institute at Cornell for Nanoscale Science, Ithaca, New York 14853, United States

Supporting Information

ABSTRACT: **Exfoliation of large-area monolayers is important for fundamental research and technological implementation of transition-metal dichalcogenides. Various techniques have been explored to increase the exfoliation yield, but little is known about the underlying mechanism at the atomic level. Here, we demonstrate gold-assisted mechanical exfoliation of monolayer molybdenum disulfide, up to a centimeter scale. Detailed spectroscopic, microscopic, and first-principles density functional theory analyses reveal that strong van der Waals (vdW) interaction between Au and the topmost MoS_2 layer facilitates the exfoliation of monolayers. However, the large-area exfoliation promoted by such strong vdW interaction is only achievable on freshly prepared clean and smooth Au surfaces, while rough surfaces and surfaces exposed to air for more than 15 min result in negligible exfoliation yields. This technique is successfully extended to $MoSe_2$, WS_2, WSe_2, $MoTe_2$, WTe_2, and GaSe. In addition, electrochemical characterization reveals intriguing interactions between monolayer MoS_2 and Au. A subnanometer-thick MoS_2 monolayer strongly passivates the chemical properties of the underlying Au, and the Au significantly modulates the electronic band structure of the MoS_2, turning it from semiconducting to metallic. This could find applications in many areas, including electrochemistry, photovoltaics, and photocatalysis.**

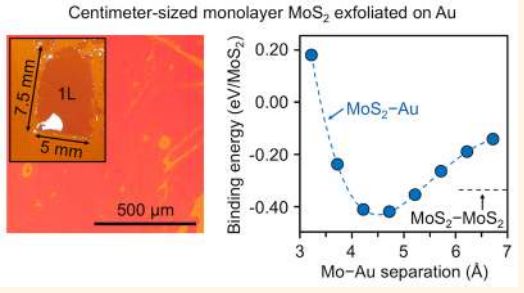

KEYWORDS: *transition-metal dichalcogenide, MoS_2, gold, monolayer, exfoliation, electrochemical, mechanism*

Monolayer transition-metal dichalcogenides (TMDCs) possess a wide range of extraordinary optoelectronic, chemical, and mechanical properties unattainable in their bulk form.[1−3] Many bulk TMDCs are semiconductors with an indirect band gap, which transitions to a direct band gap when in monolayer form, rendering them excellent materials for optoelectronics.[4−6] A major challenge for large-scale application of TMDCs is the competition between material quality and production scalability. For instance, readily scalable liquid-phase exfoliation is tainted by the small size, poor quality, and contamination of the resulting crystals.[7] Chemical vapor deposition yields large-area monolayers, but their quality is inferior to those made by mechanical exfoliation (ME), and the method is time-consuming and costly.[8] By contrast, ME generally yields the highest quality monolayer TMDCs, however, their typical lateral dimensions are in the range of tens to hundreds of microns.[9,10] This poses a significant challenge since many characterization techniques, large-scale processing, and applications typically require macroscopic samples. Finding a facile way of producing

Received: August 10, 2018
Accepted: September 28, 2018
Published: September 28, 2018

Downloaded via QUEEN'S UNIV OF BELFAST on October 31, 2018 at 13:42:16 (UTC).
See https://pubs.acs.org/sharingguidelines for options on how to legitimately share published articles.

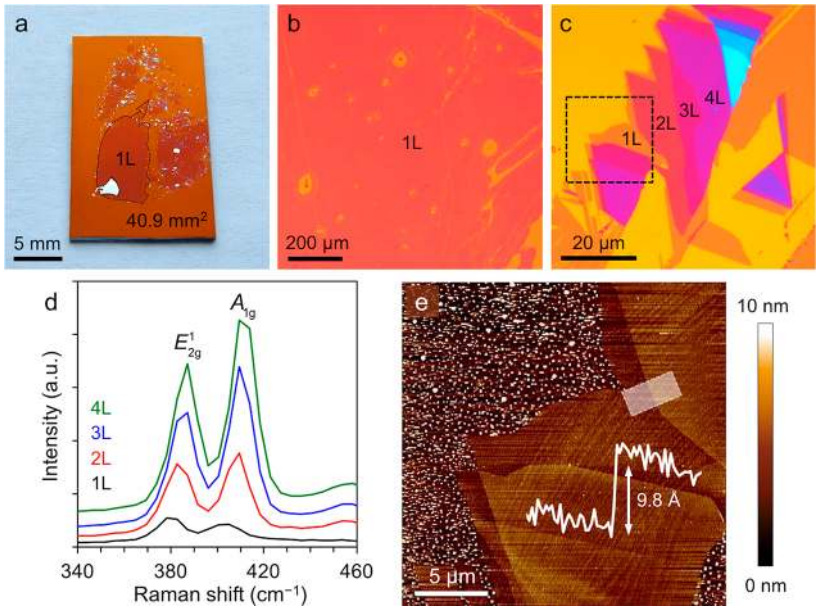

Figure 1. Exfoliation and characterization of MoS_2 on Au substrate. (a) Optical macrograph of a large-area monolayer MoS_2 on a 7.5 nm Au/1 nm Ti/93 nm SiO_2/Si wafer. (b) Optical micrograph of a large-area monolayer MoS_2. (c) High-resolution optical micrographs of the mono- and multilayer MoS_2. (d) Raman spectra (532 nm excitation) of mono- and multilayer MoS_2 in (c), showing the main in-plane (E^1_{2g}) and out-of-plane (A_{1g}) vibrational modes (spectra are offset for clarity). (e) AFM topography image taken from the area highlighted in (c) by the black square, showing a smooth MoS_2 surface and tape residue on the Au surface. Inset: the corresponding height profile of monolayer−bilayer boundary, taken from the area highlighted by the white rectangle.

large, high-quality monolayer TMDCs is therefore crucial for both fundamental research and technology advancement.

Various techniques have been explored to improve the exfoliation yield. Gold is known to have a strong affinity for sulfur, which has been exploited to enhance the exfoliation of monolayer molybdenum disulfide.[11,12] However, little detail about the underlying mechanism was provided, and the largest MoS_2 size was limited to a few hundreds of microns. A comprehensive understanding of the gold-assisted large-area exfoliation at the atomic level is therefore necessary for devising techniques for the mass production of macroscopic TMDC monolayers, whose small lateral size has previously limited research and technological developments.

Here, we present a facile gold-assisted mechanical exfoliation of extraordinarily large monolayer MoS_2, up to a centimeter size (Figure 1), and provide detailed investigation on the exfoliation mechanism. Raman spectroscopy, photoluminescence (PL) measurements, X-ray photoelectron spectroscopy (XPS), and scanning transmission electron microscopy (STEM) collectively reveal that the high-yield exfoliation is facilitated by van der Waals (vdW) interaction between the Au surface and the topmost MoS_2 layer. This interaction is stronger than the interlayer vdW interactions in bulk MoS_2, therefore facilitating the exfoliation of large-area monolayer films. The cleanliness and smoothness of the Au surface are critical for the near-unity yield of monolayer MoS_2, which can only be achieved on freshly deposited Au films exposed to air for <6 min. The short air exposure prevents the accumulation of airborne organic contaminants on the Au surface, which otherwise weakens the vdW forces between MoS_2 and Au and suppresses the exfoliation. The exfoliation yield also decreases significantly with increasing surface roughness of Au. These findings are confirmed by calculations from the first-principles density functional theory (DFT). The calculated vdW binding energies of several MoS_2/Au heterostructures, with varied Au−Mo separations and surface roughness, show excellent agreement with the experiments. We successfully applied this exfoliation technique to a variety of metal chalcogenides, including $MoSe_2$, WS_2, WSe_2, $MoTe_2$, WTe_2, and GaSe (Supporting Figure S1), and found that the monolayer yield is generally near-unity, limited only by the size of the parent bulk crystal.

We further discovered intriguing interactions between monolayer MoS_2 and the underlying Au. Electrochemical characterization, using voltammetry and scanning electrochemical microscopy (SECM), reveals that the surface density of electronic states (DOS) of MoS_2 is strongly modulated by the underlying Au and, conversely, that the Au substrate is endowed with the chemical properties of MoS_2. This is manifested in strong passivation of the Au surface by the physisorbed monolayer MoS_2 for inner-sphere electron transfer, while the outer-sphere electron transfer is almost unaffected due to long-range electron tunneling. These intriguing properties bring opportunities for many applications in areas such as electrode modification and energy storage/conversion.

RESULTS

Exfoliation and Characterization of MoS_2 on Au. Figure 1a shows a macroscopic optical image of MoS_2 exfoliated on a 7.5 nm-thick Au (111) grown by physical vapor deposition (PVD) on a SiO_2/Si wafer with a 1 nm Ti adhesion layer. MoS_2 monolayers reach lateral dimensions close to 1 cm, limited only by the size and quality of the parent bulk crystal. The microscopic optical image in Figure 1b reveals good crystal uniformity with occasional breaks likely caused by lattice defects, surface contamination, and mechanical stress during exfoliation. The number of MoS_2 layers was unambiguously determined using optical microscopy, Raman spectroscopy, and atomic force microscopy

DOI: 10.1021/acsnano.8b06101
ACS Nano 2018, 12, 10463−10472

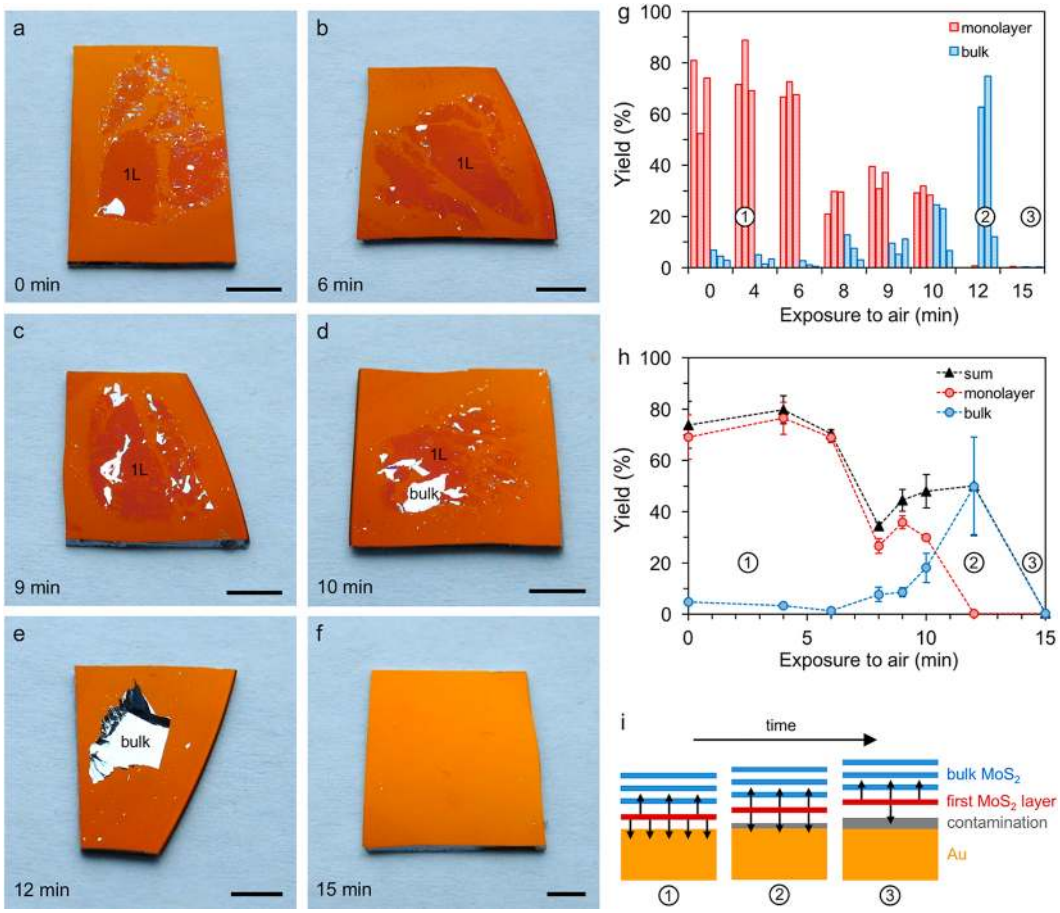

Figure 2. Dependence of the MoS_2 exfoliation yield on exposure to air. (a–f) Optical macrographs of MoS_2 exfoliated on 7.5 nm Au at different times after the Au exposure to air. All scale bars correspond to 5 mm. (g) Quantification of the monolayer (red) and bulk (blue) yields at different times (columns are yields at different areas of the sample). (h) Dependence of the average yield with time for monolayer (red circles), bulk (blue circles), and the sum of the two (black triangles). A constant area of 0.25 cm^2 (0.5 × 0.5 cm^2) was used in all quantifications. (i) Schematic depiction of the evolution of the adhesion forces between different surfaces with the three limiting cases (1–3) assigned in (g–h). Note that the 0 min exfoliation was done immediately (within 10–15 s) after removal of the freshly grown Au from the vacuum chamber load-lock.

(AFM). The high optical contrast of monolayer MoS_2 allows direct counting of the layers (Figure 1c). The Raman spectra in Figure 1d show the two main vibrational modes, E^1_{2g} (in-plane) and A_{1g} (out-of-plane), whose intensities increase monotonically with increasing number of MoS_2 layers (≤4L), as expected.[13] The frequency of both modes blueshifts with the increasing MoS_2 thickness, which is attributed to a stiffening of the vibrations upon layer addition. An anomalous redshift of the E^1_{2g} mode, due to stacking-induced changes in intralayer bonding, is often observed on insulating substrates.[10,13,14] Here we observe a blueshift of the E^1_{2g} mode, suggesting a strong interaction between MoS_2 and Au, which leads to an efficient charge transfer and screening of the long-range Coulomb interactions between MoS_2 layers. This is also consistent with the large frequency shifts of 8–10 cm^{-1} between the 1L and 4L MoS_2. AFM topography imaging across a monolayer–bilayer boundary gives a step-height of 9.8 Å (insets in Figure 1e), which is slightly higher than the theoretical thickness of 6.15 Å,[3] but in agreement with the literature.[13,15] No PL was observed in monolayer MoS_2 on Au (Supporting Figure S2) since it is completely quenched due the conformal contact between MoS_2 and Au, consistent with previous reports.[16] The occasional observation of PL in monolayer MoS_2 on Au[17,18] could be caused by an increased physical separation due to polymer residues and airborne contaminants at the MoS_2/Au interface.

Mechanism of the Large-Area Exfoliation. We found that the exfoliation critically depends on the surface condition of Au, governed specifically by the Au roughness and the aging of the Au surface since its deposition under ultrahigh vacuum. The average area yield of exfoliation, expressed as the percentage of Au surface covered with MoS_2 (see Methods), is large (70–80%, predominantly monolayer) on freshly prepared Au, but gradually decreases with the time of Au exposed to air, with an increasingly larger proportion of bulk MoS_2 (Figure 2). After 15 min, almost no crystals are exfoliated (yield <0.5%). This suggests that the adhesion forces between MoS_2 and Au strongly depend on how long the Au surface has aged in air, which we summarize in the following three stages (Figure 2g–i): Initially (1), the adhesion between Au and the first MoS_2 layer is stronger than the interaction between the first MoS_2 layer and the rest of MoS_2, resulting in the predominant exfoliation of monolayer MoS_2. Gradually (2), the MoS_2–Au adhesion weakens and becomes comparable to the interlayer interactions in bulk MoS_2, facilitating more efficient exfoliation of thicker MoS_2 (governed by lattice defects), giving rise to a peak in the bulk yield (Figure 2g–h). In the end (3), the MoS_2–Au adhesion becomes weaker than

DOI: 10.1021/acsnano.8b06101
ACS Nano 2018, 12, 10463–10472

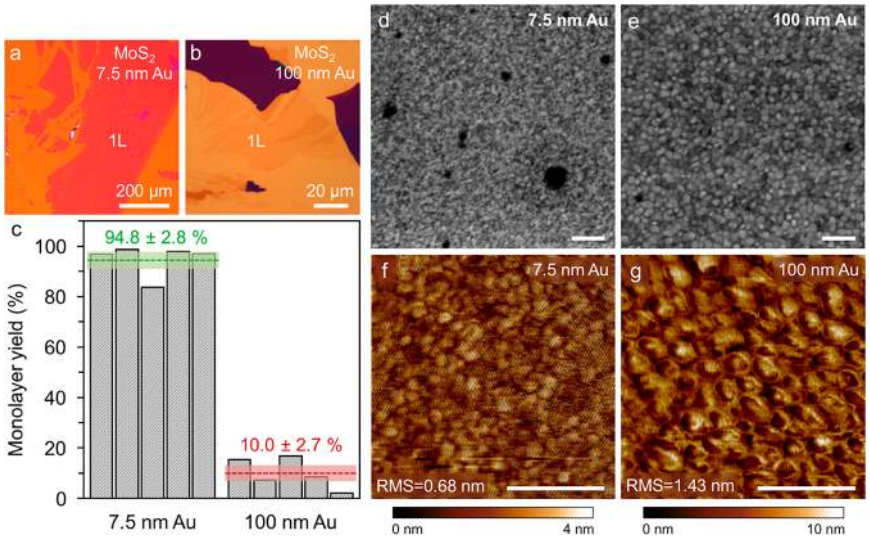

Figure 3. Dependence of monolayer MoS_2 exfoliation yield on Au roughness. (a–b) Optical micrographs of MoS_2 exfoliated on 7.5 and 100 nm Au, respectively. (c) Quantification of the monolayer yield for 7.5 and 100 nm Au. A constant area of 12,100 μm^2 (110 × 110 μm^2) was used in all quantifications. (d–e) SEM images of 7.5 and 100 nm Au substrates, showing continuous polycrystalline Au coverage with occasional voids and grain sizes varying from 10–20 nm to 40–60 nm for 7.5 to 100 nm-thick Au, respectively. (f–g) AFM images of the same substrates taken immediately after Au deposition, showing indentations within the grains of 100 nm Au and the measured RMS roughness of the surface. Scale bars in (d–g) correspond to 200 nm.

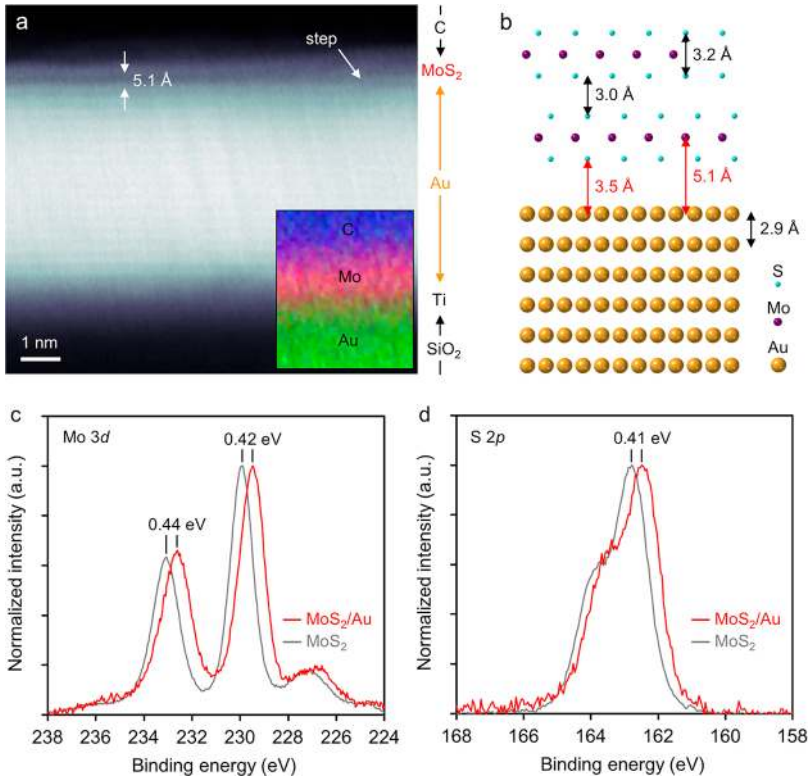

Figure 4. STEM and XPS characterization of monolayer MoS_2 on Au. (a) HAADF-STEM image of monolayer MoS_2 on 5 nm Au showing a region of clean MoS_2/Au interface with an average Mo–Au separation of 5.1 Å. Inset: EELS composite image acquired from the middle region of the image, confirming the presence of Au, Mo, and C. (b) A schematic structure model of the MoS_2/Au heterostructure. The distances in red are determined from HAADF-STEM, and the distances in black are the lattice parameters of bulk MoS_2 and Au.[3,30] (c–d) High-resolution XPS of Mo 3*d* and S 2*p* regions of monolayer MoS_2/Au (red) and bulk MoS_2 (gray), showing a shift in the binding energy due to charge transfer. The binding energies were obtained from Gaussian fits of the baseline-subtracted Mo 3*d* and S 2*p* spectra.

the interlayer interaction in bulk MoS_2, and the exfoliation yield is negligible.

The above phenomenon is caused by the adsorption of organic airborne contaminants, which transform the freshly deposited Au surface from hydrophilic to hydrophobic. This was shown by Smith, who confirmed that while a clean Au surface is hydrophilic, exposure to air (but also prolonged dwell time under vacuum) leads to the build-up of a

DOI: 10.1021/acsnano.8b06101
ACS Nano 2018, 12, 10463–10472

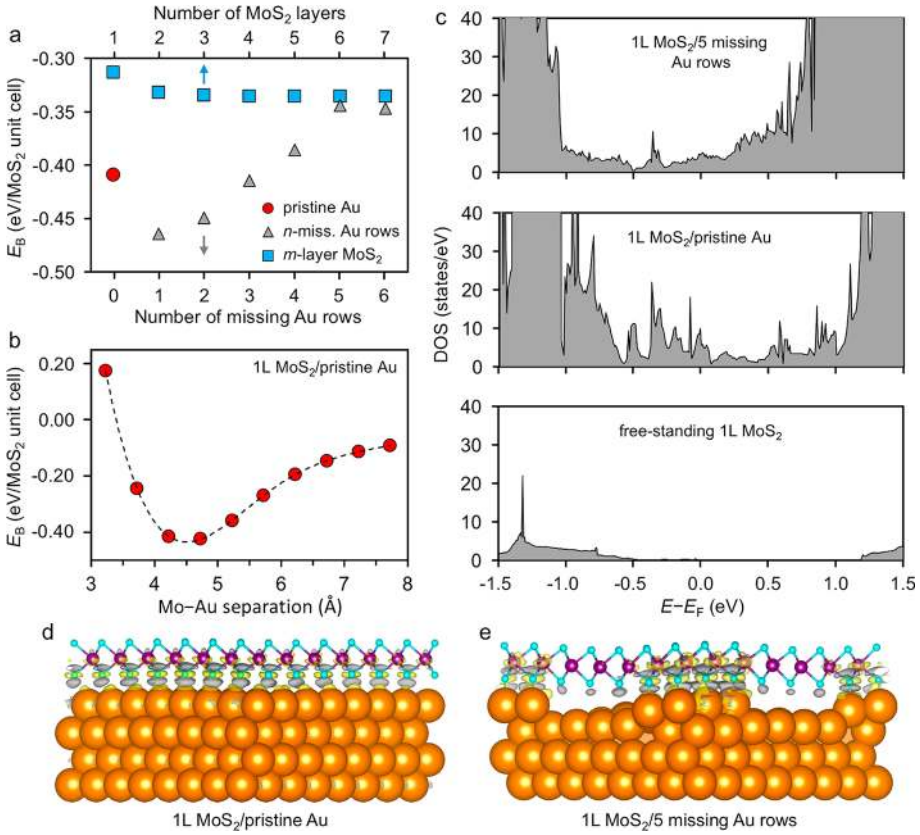

Figure 5. vdW DFT calculations of the MoS_2–Au interactions. (a) Binding energies determined for several different systems of monolayer MoS_2 on: pristine Au (111), Au (111) with a different number (n) of missing Au rows, and m-layer MoS_2. (b) Binding energy of monolayer MoS_2 on pristine Au as a function of the separation between Mo and Au atomic planes. The equilibrium separation was determined to be 4.5 Å, in good agreement with the experimental value from HAADF-STEM. (c) DOS for free-standing monolayer MoS_2 (bottom panel), monolayer MoS_2 on pristine Au (middle panel), and monolayer MoS_2 on Au with 5 missing Au rows (top panel). (d–e) Charge density differences calculated for monolayer MoS_2 on: pristine Au (111) (d), 5 missing Au rows (e), plotted as $\Delta\rho = \rho[\text{Au} + \text{MoS}_2] - \rho[\text{Au}] - \rho[\text{MoS}_2]$, where the three latter terms are the total charge densities of monolayer MoS_2/Au, Au slab, and monolayer MoS_2, respectively.

submonolayer of carbonaceous contamination, which quickly turns the Au surface hydrophobic.[19] This was manifested by an abrupt increase of the water contact angle (WCA) on Au by about 30°–40° within 10 min. Indeed, we found that the WCA on Au exposed to air rapidly increases by 15°–30° in the first 15 min (Supporting Figure S3), following the same trend as the exfoliation yield (Figure 2). The contamination layer increases the separation between MoS_2 and Au, weakens the adhesion forces between the two, and consequently reduces the exfoliation yield.

We further found that the yield of monolayer MoS_2 notably decreases with increasing thickness of the Au films, as shown in Figure 3a–c for 7.5 and 100 nm-thick Au. The scanning electron microscopy (SEM) images in Figure 3d–e show that the surface of the 7.5 nm Au is smoother than that of the 100 nm Au, which is further quantified by the AFM topography images in Figure 3f–g. The higher surface roughness of the thicker Au film therefore appears to weaken the vdW interactions between Au and MoS_2, due to increased physical separation at surface depressions, also supported by theoretical calculations below. The best exfoliation results are achieved on thin Au films of 5–20 nm with root-mean-square (RMS) roughness <1 nm. Despite the polycrystalline nature of the Au films evident from SEM and AFM, the predominant crystal orientation was found to be Au (111) by X-ray diffraction (XRD) measurements (Supporting Figure S4). This is typical for Au PVD films grown on various substrates, using different deposition conditions,[20−22] and expected from the lowest energy of the Au (111) surface.[23]

The Nature of MoS_2–Au Interaction. The MoS_2 interaction with Au was predicted to be of vdW nature due to weak hybridization.[24,25] However, few have provided direct experimental evidence of the Au-MoS_2 interaction. Here we employed STEM to image the separation between monolayer MoS_2 and Au. The left-hand side of the high-angle annular dark-field (HAADF)-STEM image in Figure 4a shows a region of a clean monolayer MoS_2/Au interface. The average closest separation between the center of the Mo and Au planes is 5.1 ± 0.3 Å, close to the value of 4.5 Å obtained from theoretical calculations below. This implies a 3.5 Å spacing between the Au and S planes, ∼17% larger than the interlayer vdW spacing in bulk MoS_2 (3.0 Å) and ∼59% larger than a covalent Au–S bond (2.2 Å),[3,26] confirming that the MoS_2–Au interaction is strong vdW rather than covalent in nature. Monolayer MoS_2 maintains the spacing due to its conformity with the underlying Au, as seen from the step in the top-right area of Figure 4a. A schematic model of the MoS_2/Au heterostructure is shown in Figure 4b.

We also employed XPS to further investigate the interaction between MoS_2 and Au. The high-resolution spectra of the Mo 3d and S 2p regions in Figure 4c–d reveal that the binding energies in monolayer MoS_2 decrease by ∼0.4 eV in

DOI: 10.1021/acsnano.8b06101
ACS Nano 2018, 12, 10463–10472

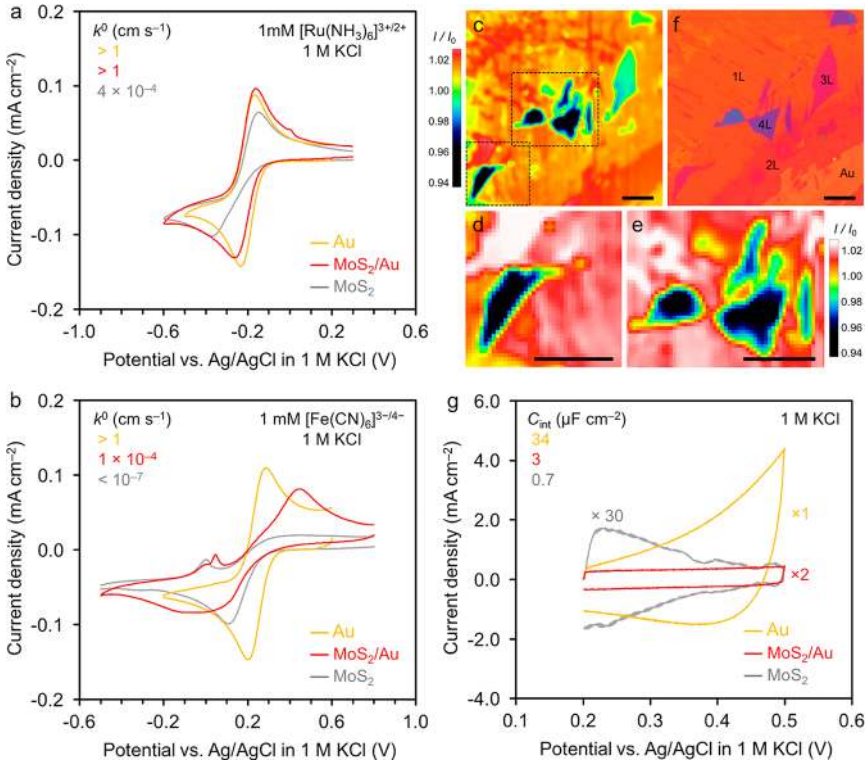

Figure 6. Electrochemical characterization of MoS_2 on Au. (a–b) Cyclic voltammograms of 1 mM $[Ru(NH_3)_6]^{3+/2+}$ and 1 mM $[Fe(CN)_6]^{3-/4-}$ reduction/oxidation in 1 M KCl at 50 mV s^{-1}, respectively. Results for the bare Au surface (gold), monolayer MoS_2/Au (red), and bulk MoS_2 (gray) are shown. (c) SECM image of different MoS_2 layers on Au, generated in feedback mode using 1 mM $[Ru(NH_3)_6]^{3+/2+}$ in 0.1 M KCl. (d–e) Magnified SECM images taken from regions highlighted in (c) by the black rectangles. (f) Corresponding optical image of the measured area. All scale bars correspond to 40 μm. (g) Cyclic voltammograms in 1 M KCl at 50 V s^{-1} for the determination of the interfacial capacitance. All measurements were carried out under ambient light at room temperature, and argon-deaerated solutions were used in (a–b) and (g).

comparison to bulk MoS_2. This suggests that there is a significant degree of charge transfer between monolayer MoS_2 and Au, consistent with the observed PL quenching. Almost identical shifts (0.4–0.5 eV) were observed in other MoS_2–Au systems and explained by the formation of a Schottky barrier at the MoS_2/Au interface[27] and charge transfer from Au to MoS_2, leading to an increase of the electron density at the interface.[28,29] Crucially, the lack of changes in the shape and width of the XPS peaks in our work confirms that monolayer MoS_2 maintains its chemical identity upon exfoliation (detailed XPS spectra including the peak fittings are shown in Supporting Figure S5).

To further elucidate the interaction between monolayer MoS_2 and Au, we performed first-principles atomistic calculations for a range of systems. Figure 5a shows the binding energy (E_B, per MoS_2 unit cell) for monolayer MoS_2 on different systems: pristine Au (111) surface, Au surface with n missing Au rows, and on m-layer MoS_2. The calculations suggest E_B = −0.41 eV for monolayer MoS_2 on pristine Au (Figure 5a), which is stronger than the binding between monolayer MoS_2 and bulk MoS_2 (E_B = −0.34 eV for $m \geq 5$), supporting the predominant exfoliation of monolayers, in agreement with our earlier interpretation and other theoretical calculations.[25,31] The binding energy between Au and MoS_2 rapidly decreases with increasing Au–MoS_2 separation (Figure 5b), explaining why a submonolayer contamination significantly inhibits the exfoliation.

Introduction of a small number of surface Au vacancies or adatoms is found to have negligible effects on the binding energy (−0.42 eV). Conversely, when a large vacancy in the form of n missing surface rows is introduced to the Au surface, the binding energy changes significantly. As shown in Figure 5a, the E_B is initially high for n = 1 but decreases to reach a similar magnitude to that of pristine Au for n = 3. The increased number of active sites with large amount of dangling bonds and charge density at the Au surface initially leads to stronger Au–S interaction, as seen for $n \leq 3$. For $n > 3$, the comparably poorer conformity of MoS_2 to Au weakens this interaction, which becomes comparable to that of bulk MoS_2 for n = 5 and 6. These calculations are consistent with the observation that the smooth, thin Au can produce large-area exfoliation, while the rougher, thicker Au cannot. This reinforces our conclusion that the surface quality of Au is critical for the success of large-area exfoliation.

The most striking difference occurs in the electronic structure of MoS_2. The semiconducting character of free-standing MoS_2 changes to metallic in the monolayer MoS_2/Au heterostructure (Figure 5c). Indeed, the Bader charge analysis indicates a system-dependent electron transfer from Au to the monolayer MoS_2 (Supporting Figure S6). The resulting increase of the DOS at the Fermi level (E_F) has a direct impact on the electrochemical behavior discussed below. These states, which originate mainly from S 3s–p orbitals and Mo 4d orbitals, reside at the MoS_2/Au interface (Figure 5d–e).

Electrochemical Characterization of the MoS_2–Au Heterostructure. The large-area monolayer MoS_2 on Au is an excellent platform for investigations previously limited by

DOI: 10.1021/acsnano.8b06101
ACS Nano 2018, 12, 10463–10472

the small lateral crystal size. Figure 6 shows the electrochemical characterization of three macroscopic (~0.5 mm^2) surfaces: bare Au (gold), monolayer MoS_2/Au (red), and bulk MoS_2 (gray). The kinetics of the reduction/oxidation of $[Ru(NH_3)_6]^{3+/2+}$ and $[Fe(CN)_6]^{3-/4-}$ used as redox mediators, quantified by the heterogeneous electron-transfer rate constant (k^0), vary greatly on these surfaces, as illustrated by the voltammograms in Figure 6a–b. Au exhibits the fastest, reversible kinetics for both mediators ($k^0 > 1$ cm s^{-1}), expected due to their fast self-exchange rates and the high DOS of Au. The k^0 values on bulk MoS_2 are ~4×10^{-4} cm s^{-1} and <10^{-7} cm s^{-1} for $[Ru(NH_3)_6]^{3+/2+}$ and $[Fe(CN)_6]^{3-/4-}$, respectively, in agreement with previous work.[32] The kinetics of $[Ru(NH_3)_6]^{3+/2+}$, which is thought to be an outer-sphere mediator only sensitive to the surface DOS, are reversible on monolayer MoS_2/Au and similar to that of bare Au (Figure 6a), indicating strong electronic coupling and charge transfer between MoS_2 and Au, in agreement with our results above. The SECM imaging of the $[Ru(NH_3)_6]^{3+/2+}$ redox activity of MoS_2 on Au (Figure 6c–e) shows a clear correlation with the corresponding optical image (Figure 6f). As the number of MoS_2 layers decreases, the normalized current (I/I_0) increases, indicating a transition from the semiconducting multilayer MoS_2 to the metallic monolayer MoS_2/Au in agreement with the predicted increase in DOS (Figure 5f), with the highest current observed for the bare Au. In contrast, the kinetics of $[Fe(CN)_6]^{3-/4-}$ on monolayer MoS_2/Au slows down by 6 orders of magnitude to ~1×10^{-4} cm s^{-1} within the quasi-reversible regime (Figure 6b). The strong suppression of the kinetics of $[Fe(CN)_6]^{3-/4-}$, which is an inner-sphere mediator interacting strongly with the electrode surface, indicates that the Au surface is strongly passivated by the MoS_2 monolayer. In addition, the open circuit potential in 1 M KCl was found to be the same for monolayer MoS_2/Au and bulk MoS_2 (0.000 V), but considerably different for Au (0.034 V). No dependence on illumination was observed for monolayer MoS_2/Au, as expected. These results suggest that monolayer MoS_2/Au is chemically similar to MoS_2 but has an increased DOS acquired from the underlying Au. In other words, monolayer MoS_2/Au is thermodynamically closer to bulk MoS_2 but kinetically closer to Au. These characteristics could be effectively used to discriminate between the outer- and inner-sphere electron-transfer mechanisms. A similar concept of electronic modulation was recently demonstrated for graphene on Au.[33]

Capacitance measurements in 1 M KCl also reveal significant differences between the three surfaces (Figure 6g). The interfacial (measured) capacitance C_{int} is a sum of two capacitances in series: $C_{int}^{-1} = C_{SC}^{-1} + C_{EDL}^{-1}$, where C_{SC} and C_{EDL} are the space charge and electrical double-layer capacitances at the electrode/liquid interface.[34] C_{int} = 34 μF cm^{-2} for bare Au and is equal to C_{EDL} due to the efficient Thomas-Fermi screening in metals ($C_{SC} \gg C_{EDL}$). C_{int} = 0.7 μF cm^{-2} in bulk MoS_2 and is equal to C_{SC}, since in semiconductors $C_{SC} \ll C_{EDL}$. An intermediate C_{int} = 3 μF cm^{-2} in monolayer MoS_2/Au is mostly dominated by C_{SC} ($C_{int} \approx 0.9C_{SC}$, calculated using the C_{EDL} determined for Au). The shapes of the voltammograms in Figure 6g reflect the differing electronic band structures of the three different surfaces. The metallic Au behaves as a typical pseudocapacitor with a redox (faradaic) activity superimposed over the double-layer charging at high potentials. The response of bulk MoS_2 is typical for an n-type semiconductor, with the higher currents at low potentials corresponding to the charge carrier accumulation regime. Surprisingly, monolayer MoS_2/Au exhibits a rectangular-shaped voltammogram, indicating a purely capacitive (nonfaradaic) response, which originates solely from the double-layer charging. Such potential-independent capacitance response, which is typical of an electrochemical supercapacitor,[35,36] is significantly different from the responses of bulk MoS_2 and bare Au. This suggests that monolayer MoS_2/Au system (and potentially many other TMDCs/Au) could provide an interesting platform for the design of supercapacitors and other devices for electrochemistry, photocatalysis, and energy storage/conversion.

CONCLUSIONS

We present a facile gold-assisted mechanical exfoliation of extraordinarily large monolayer MoS_2, up to a centimeter-scale, limited mainly by the parent bulk crystal size. We carried out detailed spectroscopic and microscopic characterizations together with first-principles DFT calculations to provide an atomic-level understanding of the exfoliation mechanism. The large-area exfoliation is found to be facilitated by strong vdW interaction between Au and the topmost layer of MoS_2, which critically depends on the cleanliness and smoothness of the Au surface. Near-unity yield of monolayer MoS_2 is achieved on freshly grown thin Au films (5–20 nm) with RMS roughness <1 nm and exposure to air for <6 min. The yield becomes negligible after 15 min of exposure due to the accumulation of airborne contamination on Au. Such previously unknown stringent experimental conditions have important consequences for the development of large-area exfoliation and growth techniques. We have successfully extended the technique to $MoSe_2$, WS_2, WSe_2, $MoTe_2$, WTe_2, and GaSe. Electrochemical characterization reveals that the surface DOS of monolayer MoS_2 is strongly modulated by the underlying Au, turning it from semiconducting to metallic. Conversely, the subnanometer-thick monolayer MoS_2 strongly passivates the chemistry of the underlying Au electrode, but does not prevent charge transfer from solution to Au. Our work sheds light on the mechanism of gold-assisted exfoliation, provides important guidance for the production of macroscopic TMDC monolayers, and has important implications for many research areas, such as electrode modification, photovoltaics, and photocatalysis.

METHODS

Materials Preparation. PVD films were prepared with a DC magnetron sputtering system (Kurt J. Lesker CMS-A) using targets (>99.99%) from Testbourne Ltd. (Ti) and Birmingham Metal Ltd. (Au). The SiO_2/Si wafers (IDB Technologies Ltd.) were cleaned in acetone and isopropanol and blow-dried before placing in a load-lock, evacuated to ~10^{-7} Torr by a turbomolecular pump (Shimadzu TMP-303LM) backed by a mechanical pump (Adixen ACP 15). They were then transferred to the deposition chamber, evacuated to ~10^{-9} Torr using a cryopump (Brooks CTI-Cryogenics 10F). All the pumps were oil-free, and the residual gas environment was continuously monitored by mass spectrometry prior to the sputtering. Depositions were done at room temperature under a 5 SCCM Ar flow at partial pressure of 10^{-3} Torr. A Ti adhesion layer was deposited at 15° incidence at a rate of 0.5 Å s^{-1} before the Au deposition. The Au layer was deposited at a 33° incidence at a rate of 1.5 Å s^{-1}. Both targets were presputtered prior to the deposition. All metal chalcogenides were exfoliated from bulk crystals (Manchester Nanomaterials Ltd.) directly onto the Au substrates using the "scotch-tape" method reported elsewhere,[37] applying a downward pressure, rather than lateral rubbing. The crystals were exfoliated, and therefore exposed to air, immediately prior to the contact with Au (<5 s) in order to

DOI: 10.1021/acsnano.8b06101
ACS Nano 2018, 12, 10463–10472

minimize the airborne contamination of their surface. Bulk crystals were either natural (molybdenite) or synthesized by chemical vapor transport ($MoSe_2$, $MoTe_2$, WS_2, WSe_2, WTe_2, and GaSe). The exfoliation and subsequent characterization (except the vacuum techniques) were performed at 20−23 °C and 50−70% relative humidity.

Microscopy, Spectroscopy, Reflectivity, and Diffraction Characterization. Macroscopic optical images were taken using a Canon PowerShot A720 IS digital camera. Microscopic optical images were taken using a BX51 microscope (Olympus Corp) with an Infinity2-2 CCD camera and Infinity Capture 6.2 software (Lumenera Corp). The exfoliation yield should ideally be calculated as the ratio between the area of the exfoliated film and the contact surface area of parent MoS_2 crystals. However, as the size of the parent crystals and their surface defect and impurity densities vary for different exfoliations, such approach is impractical. To circumvent this uncertainty, we used a constant sampling area (rather than the actual parent crystal size) for each yield comparison. For Figure 2, identical square areas of 0.5 × 0.5 cm^2 were chosen at three different locations on each of the sample using Fiji/ImageJ software (v.2.0) to maximize the area of exfoliated MoS_2 films inside the square boxes. The exfoliation yield (Y) was then calculated as Y (%) = A_M/A_S × 100%, where A_M is the area of exfoliated MoS_2 inside each of the square box and A_S is the sampled area. The results are shown in Figure 2g. Similarly, a sampling area of 110 × 100 μm^2 was used to calculate the roughness-dependent exfoliation yields in Figure 3. Such a method allows meaningful quantitative comparison of the yield dependence on the surface condition of Au and provides a quantitative assessment of the capability of the technique. 532 or 633 nm lasers of 1 mW power focused through a 100× MPlan N objective (Olympus Corp) to ∼1 μm^2 spot size were used for Raman spectroscopy and PL measurements, collected by a Jobin Yvon HR640 Raman spectrometer and Andor MCD 2.6 software. AFM measurements were performed with a Digital Instruments Veeco Dimension 300 AFM with 30 nm Si-SPM tips (Nanosensors) in tapping mode. The contact angle measurements were carried out using a Dino-Lite Edge AM7115MZTL Digital microscope and in-house rotating-state goniometer. A field emission JEOL JSM-6500F SEM at an accelerating voltage of 5−10 kV was used for SEM imaging. The X-ray reflectivity and XRD, taken using a D8 Discover diffractometer (Bruker Inc.), were used to determine the thickness and crystallographic orientation of Au, respectively. XPS was performed using a nonmonochromatic Mg K_α source, collecting the photoelectrons at glancing incidence from the surface normal, from an area of ∼0.8 cm^2. The spectrometer energy analyzer work function was calibrated using an Ag standard. Tougaard baseline subtraction and normalization to the maximum intensity were applied to all spectra. STEM samples were prepared in a FEI Strata 400 focused ion beam using a standard cross-section fabrication procedure.[38] STEM and electron energy loss spectroscopy (EELS) imaging were performed using a NION UltraSTEM operated at 100 keV.

Computational Methods. First-principles *ab initio* calculations were carried out with the Vienna *ab initio* simulation package.[39] The generalized gradient approximation along with the Tkatchenko−Scheffler method were used to correct the energy due to dispersion interactions.[40,41] This was used along with a 345 eV plane-wave cutoff. The projector augmented wave pseudopotentials were utilized to model the bonding environment between atoms.[42,43] Energy convergence for the electronic and ionic minimizations was set at 1 × 10^{-5} and 1 × 10^{-4} eV, respectively. Au (111) and monolayer MoS_2 unit cells were relaxed with a 12 × 12 × 6 and 12 × 12 × 1 Γ-centered k-grid, respectively. From this an 8 × 8 × 4 Au surface was created as well as a 7 × 7 × 1 MoS_2 supercell. This resulted in ∼1.0% lattice mismatch, which was applied to the Au surface to avoid spurious variation on the strain sensitive MoS_2 energetics. The bottom two Au layers were fixed as bulk, while the top two Au layers, representing the surface, were allowed to relax. After the introduction of defects, the Au surface was allowed to relax further. The MoS_2 supercell was then placed on top of the Au surface, and the MoS_2/Au heterostructure was allowed to relax once again. Binding energies of 1L MoS_2 on m-layer MoS_2 were calculated as $E_B = E_{(m+1)L} - E_{mL} - E_{1L}$, where $E_{(m+1)L}$, E_{mL}, and E_{1L} are the total energies of $(m + 1)$-, m-, and 1-layer MoS_2, respectively. Binding energies of 1L MoS_2 on Au systems were calculated as $E_B = E_{1L+Au} - E_{Au} - E_{1L}$, where E_{1L+Au} and E_{Au} and are the total energies of 1L MoS_2 on Au and the Au slab, respectively.

Electrochemical Measurements. All electrochemical measurements were performed using a CHI920D potentiostat (CH Instruments, Inc.). The electrochemical setup is schematically shown in Supporting Figure S7. The k^0 values were estimated from the peak-to-peak separation in the voltammograms (10−400 mV s^{-1}). This was done using the Nicholson method and the Klingler−Kochi method in the reversible-quasireversible and irreversible regime, respectively, following the methodology reported elsewhere (eqs (1) and (2) in ref 44, respectively). Diffusion coefficients of 7.4 (5.3) × 10^{-6} cm^2 s^{-1} and 7.7 (6.2) × 10^{-6} cm^2 s^{-1} for the oxidized (reduced) forms of $[Ru(NH_3)_6]^{3+/2+}$ and $[Fe(CN)_6]^{3-/4-}$, respectively, were determined from voltammetry at polished 2 mm diameter Pt disk using the Randles−Ševčík equation.[35] The interfacial capacitance (C_{int}) was calculated by integrating the current over the potential range as described elsewhere and averaged for scan rates between 10−50 V s^{-1}.[45] The reference potential used here (Ag/AgCl in 1 M KCl) is +0.232 V on the standard hydrogen electrode scale, taking the activity coefficient of Cl^- into account.[46] SECM was obtained using a 1 μm diameter Pt ultramicroelectrode probe with a glass radius of ∼25 μm (Heka), operated in feedback mode at a working distance of *ca.* 1 μm. The probe potential was set to reduce/oxidize $[Ru(NH_3)_6]^{3+/2+}$ under diffusion control, while the substrate was unbiased. The probe current (I) measured near the surface was normalized to the current in bulk solution (I_0).

ASSOCIATED CONTENT

Supporting Information

The Supporting Information is available free of charge on the ACS Publications website at DOI: 10.1021/acsnano.8b06101.

Optical micrographs of various metal chalcogenide monolayers exfoliated on Au substrate; PL measurement of MoS_2 on Au; water contact angle measurement on Au as a function of its exposure to air; XRD measurement of the Au films; detailed XPS spectra including peak fittings; Bader charge-transfer analysis of MoS_2Au heterostructures; schematic of electrochemical setup (PDF)

AUTHOR INFORMATION

Corresponding Authors

*E-mail: f.huang@qub.ac.uk.
*E-mail: mv337@cornell.edu.

ORCID

Yimo Han: 0000-0003-0563-4611
Andrew J. Wain: 0000-0002-8666-6158
Melissa A. Hines: 0000-0002-7960-8208
Héctor D. Abruña: 0000-0002-3948-356X
Fumin Huang: 0000-0001-6489-9818

Notes

The authors declare no competing financial interest.

ACKNOWLEDGMENTS

This project has received funding from the UK EPSRC (grant no. EP/N025938/1), the European Union's Horizon 2020 research and innovation programme under the Marie Skłodowska-Curie grant agreement no. 746685, and the UK National Measurement System (Department of Business, Energy & Industrial Strategy) and was supported by Seagate Technology (Ireland) under SOW no. 00077300.0 and the

DOI: 10.1021/acsnano.8b06101
ACS Nano 2018, 12, 10463−10472

Royal Academy of Engineering under the Research Chairs and Senior Research Fellowships Scheme, CCMR (NSF-DMR-1719875), PARADIM (NSF-DMR-1539918), DOE CSGF (DE-FG02-97ER25308), NSF-CHE-1708025, and the Alfred P. Sloan Foundation. E.J.G.S. acknowledges the use of computational resources from the UK national high-performance computing service (ARCHER) for which access was obtained *via* the UKCP consortium (EPSRC grant ref EP/K013564/1), the UK Materials and Molecular Modelling Hub for access to THOMAS supercluster, which is partially funded by EPSRC (EP/P020194/1). The Queen's Fellow Award (M8407MPH), the Enabling Fund (A5047TSL), and the Department for the Economy (USI 097) are also acknowledged.

REFERENCES

(1) Peña-Álvarez, M.; del Corro, E.; Morales-García, Á.; Kavan, L.; Kalbac, M.; Frank, O. Single Layer Molybdenum Disulfide under Direct Out-of-Plane Compression: Low-Stress Band-Gap Engineering. *Nano Lett.* **2015**, *15*, 3139−3146.

(2) Mak, K. F.; Lee, C.; Hone, J.; Shan, J.; Heinz, T. F. Atomically Thin MoS_2: A New Direct-Gap Semiconductor. *Phys. Rev. Lett.* **2010**, *105*, 136805.

(3) Velický, M.; Toth, P. S. From Two-Dimensional Materials to Their Heterostructures: An Electrochemist's Perspective. *Appl. Mater. Today* **2017**, *8*, 68−103.

(4) Withers, F.; Del Pozo-Zamudio, O.; Mishchenko, A.; Rooney, A. P.; Gholinia, A.; Watanabe, K.; Taniguchi, T.; Haigh, S. J.; Geim, A. K.; Tartakovskii, A. I.; Novoselov, K. S. Light-Emitting Diodes by Band-Structure Engineering in van der Waals Heterostructures. *Nat. Mater.* **2015**, *14*, 301−306.

(5) Lee, H. S.; Min, S.-W.; Chang, Y.-G.; Park, M. K.; Nam, T.; Kim, H.; Kim, J. H.; Ryu, S.; Im, S. MoS_2 Nanosheet Phototransistors with Thickness-Modulated Optical Energy Gap. *Nano Lett.* **2012**, *12*, 3695−3700.

(6) Bernardi, M.; Palummo, M.; Grossman, J. C. Extraordinary Sunlight Absorption and One Nanometer Thick Photovoltaics Using Two-Dimensional Monolayer Materials. *Nano Lett.* **2013**, *13*, 3664−3670.

(7) Coleman, J. N.; Lotya, M.; O'Neill, A.; Bergin, S. D.; King, P. J.; Khan, U.; Young, K.; Gaucher, A.; De, S.; Smith, R. J.; Shvets, I. V.; Arora, S. K.; Stanton, G.; Kim, H. Y.; Lee, K.; Kim, G. T.; Duesberg, G. S.; Hallam, T.; Boland, J. J.; Wang, J. J.; et al. Two-Dimensional Nanosheets Produced by Liquid Exfoliation of Layered Materials. *Science* **2011**, *331*, 568−571.

(8) Wang, X.; Gong, Y.; Shi, G.; Chow, W. L.; Keyshar, K.; Ye, G.; Vajtai, R.; Lou, J.; Liu, Z.; Ringe, E.; Tay, B. K.; Ajayan, P. M. Chemical Vapor Deposition Growth of Crystalline Monolayer $MoSe_2$. *ACS Nano* **2014**, *8*, 5125−5131.

(9) Novoselov, K. S.; Jiang, D.; Schedin, F.; Booth, T. J.; Khotkevich, V. V.; Morozov, S. V.; Geim, A. K. Two-Dimensional Atomic Crystals. *Proc. Natl. Acad. Sci. U. S. A.* **2005**, *102*, 10451−10453.

(10) Velický, M.; Bissett, M. A.; Woods, C. R.; Toth, P. S.; Georgiou, T.; Kinloch, I. A.; Novoselov, K. S.; Dryfe, R. A. W. Photoelectrochemistry of Pristine Mono- and Few-Layer MoS_2. *Nano Lett.* **2016**, *16*, 2023−2032.

(11) Desai, S. B.; Madhvapathy, S. R.; Amani, M.; Kiriya, D.; Hettick, M.; Tosun, M.; Zhou, Y.; Dubey, M.; Ager, J. W.; Chrzan, D.; Javey, A. Gold-Mediated Exfoliation of Ultralarge Optoelectronically-Perfect Monolayers. *Adv. Mater.* **2016**, *28*, 4053−4058.

(12) Magda, G. Z.; Pető, J.; Dobrik, G.; Hwang, C.; Biró, L. P.; Tapasztó, L. Exfoliation of Large-Area Transition Metal Chalcogenide Single Layers. *Sci. Rep.* **2015**, *5*, 14714.

(13) Lee, C.; Yan, H.; Brus, L. E.; Heinz, T. F.; Hone, J.; Ryu, S. Anomalous Lattice Vibrations of Single- and Few-Layer MoS_2. *ACS Nano* **2010**, *4*, 2695−2700.

(14) Li, H.; Zhang, Q.; Yap, C. C. R.; Tay, B. K.; Edwin, T. H. T.; Olivier, A.; Baillargeat, D. From Bulk to Monolayer MoS_2: Evolution of Raman Scattering. *Adv. Funct. Mater.* **2012**, *22*, 1385−1390.

(15) Robinson, B. J.; Giusca, C. E.; Gonzalez, Y. T.; Kay, N. D.; Kazakova, O.; Kolosov, O. V. Structural, Optical and Electrostatic Properties of Single and Few-Layers MoS_2: Effect of Substrate. *2D Mater.* **2015**, *2*, 015005.

(16) Bhanu, U.; Islam, M. R.; Tetard, L.; Khondaker, S. I. Photoluminescence Quenching in Gold - MoS_2 Hybrid Nanoflakes. *Sci. Rep.* **2015**, *4*, 5575.

(17) Buscema, M.; Steele, G. A.; van der Zant, H. S. J.; Castellanos-Gomez, A. The Effect of the Substrate on the Raman and Photoluminescence Emission of Single-Layer MoS_2. *Nano Res.* **2014**, *7*, 561.

(18) Najmaei, S.; Mlayah, A.; Arbouet, A.; Girard, C.; Léotin, J.; Lou, J. Plasmonic Pumping of Excitonic Photoluminescence in Hybrid MoS_2−Au Nanostructures. *ACS Nano* **2014**, *8*, 12682−12689.

(19) Smith, T. The Hydrophilic Nature of a Clean Gold Surface. *J. Colloid Interface Sci.* **1980**, *75*, 51−55.

(20) Todeschini, M.; Bastos da Silva Fanta, A.; Jensen, F.; Wagner, J. B.; Han, A. Influence of Ti and Cr Adhesion Layers on Ultrathin Au Films. *ACS Appl. Mater. Interfaces* **2017**, *9*, 37374−37385.

(21) Adamov, M.; Perović, B.; Nenadović, T. Electrical and Structural Properties of Thin Gold Films Obtained by Vacuum Evaporation and Sputtering. *Thin Solid Films* **1974**, *24*, 89−100.

(22) Parajuli, P.; Mendoza-Cruz, R.; Santiago, U.; Ponce, A.; Yacamán, M. J. The Evolution of Growth, Crystal Orientation, and Grain Boundaries Disorientation Distribution in Gold Thin Films. *Cryst. Res. Technol.* **2018**, *53*, 1800038.

(23) Skriver, H. L.; Rosengaard, N. M. Surface Energy and Work Function of Elemental Metals. *Phys. Rev. B: Condens. Matter Mater. Phys.* **1992**, *46*, 7157−7168.

(24) Zhong, H.; Quhe, R.; Wang, Y.; Ni, Z.; Ye, M.; Song, Z.; Pan, Y.; Yang, J.; Yang, L.; Lei, M.; Shi, J.; Lu, J. Interfacial Properties of Monolayer and Bilayer MoS_2 Contacts with Metals: Beyond the Energy Band Calculations. *Sci. Rep.* **2016**, *6*, 21786.

(25) Farmanbar, M.; Brocks, G. First-Principles Study of van der Waals Interactions and Lattice Mismatch at MoS_2/Metal Interfaces. *Phys. Rev. B: Condens. Matter Mater. Phys.* **2016**, *93*, 085304.

(26) Kokkin, D. L.; Zhang, R.; Steimle, T. C.; Wyse, I. A.; Pearlman, B. W.; Varberg, T. D. Au−S Bonding Revealed from the Characterization of Diatomic Gold Sulfide. *J. Phys. Chem. A* **2015**, *119*, 11659−11667.

(27) Lince, J. R.; Carré, D. J.; Fleischauer, P. D. Schottky-Barrier Formation on a Covalent Semiconductor Without Fermi-Level Pinning: The Metal-MoS_2(0001) Interface. *Phys. Rev. B: Condens. Matter Mater. Phys.* **1987**, *36*, 1647−1656.

(28) Bruix, A.; Füchtbauer, H. G.; Tuxen, A. K.; Walton, A. S.; Andersen, M.; Porsgaard, S.; Besenbacher, F.; Hammer, B.; Lauritsen, J. V. *In Situ* Detection of Active Edge Sites in Single-Layer MoS_2 Catalysts. *ACS Nano* **2015**, *9*, 9322−9330.

(29) Shi, J.; Yang, Y.; Zhang, Y.; Ma, D.; Wei, W.; Ji, Q.; Zhang, Y.; Song, X.; Gao, T.; Li, C.; Bao, X.; Liu, Z.; Fu, Q.; Zhang, Y. Monolayer MoS_2 Growth on Au Foils and On-Site Domain Boundary Imaging. *Adv. Funct. Mater.* **2015**, *25*, 842−849.

(30) Jette, E. R.; Foote, F. Precision Determination of Lattice Constants. *J. Chem. Phys.* **1935**, *3*, 605−616.

(31) Björkman, T.; Gulans, A.; Krasheninnikov, A. V.; Nieminen, R. M. van der Waals Bonding in Layered Compounds from Advanced Density-Functional First-Principles Calculations. *Phys. Rev. Lett.* **2012**, *108*, 235502.

(32) Velický, M.; Bissett, M. A.; Toth, P. S.; Patten, H. V.; Worrall, S. D.; Rodgers, A. N. J.; Hill, E. W.; Kinloch, I. A.; Novoselov, K. S.; Georgiou, T.; Britnell, L.; Dryfe, R. A. W. Electron Transfer Kinetics on Natural Crystals of MoS_2 and Graphite. *Phys. Chem. Chem. Phys.* **2015**, *17*, 17844−17853.

(33) Hui, J.; Zhou, X.; Bhargava, R.; Chinderle, A.; Zhang, J.; Rodríguez-López, J. Kinetic Modulation of Outer-Sphere Electron

DOI: 10.1021/acsnano.8b06101
ACS Nano 2018, 12, 10463−10472

Transfer Reactions on Graphene Electrode with a Sub-surface Metal Substrate. *Electrochim. Acta* **2016**, *211*, 1016−1023.
(34) Bott, A. W. Electrochemistry of Semiconductors. *Curr. Sep.* **1998**, *17*, 87−92.
(35) Bard, A. J.; Faulkner, L. R. *Electrochemical Methods. Fundamentals and Applications*, 2nd ed.; John Wiley & Sons, Inc.: New York, 2001.
(36) Conway, B. E. *Electrochemical Supercapacitors. Scientific Fundamentals and Technological Applications*, 1st ed.; Springer Science+Business Media: New York, 1999; p 698.
(37) Novoselov, K. S.; Castro Neto, A. H. Two-Dimensional Crystals-Based Heterostructures: Materials with Tailored Properties. *Phys. Scr.* **2012**, *2012*, 014006.
(38) Giannuzzi, L. A.; Stevie, F. A. *Introduction to Focused Ion Beams: Instrumentation, Theory, Techniques and Practice*; Springer: Boston, MA, 2005.
(39) Kresse, G.; Hafner, J. *Ab initio* Molecular Dynamics for Open-Shell Transition Metals. *Phys. Rev. B: Condens. Matter Mater. Phys.* **1993**, *48*, 13115−13118.
(40) Perdew, J. P.; Burke, K.; Ernzerhof, M. Generalized Gradient Approximation Made Simple. *Phys. Rev. Lett.* **1996**, *77*, 3865−3868.
(41) Tkatchenko, A.; Scheffler, M. Accurate Molecular Van Der Waals Interactions from Ground-State Electron Density and Free-Atom Reference Data. *Phys. Rev. Lett.* **2009**, *102*, 073005.
(42) Blöchl, P. E. Projector Augmented-Wave Method. *Phys. Rev. B: Condens. Matter Mater. Phys.* **1994**, *50*, 17953−17979.
(43) Kresse, G.; Joubert, D. From Ultrasoft Pseudopotentials to the Projector Augmented-Wave Method. *Phys. Rev. B: Condens. Matter Mater. Phys.* **1999**, *59*, 1758−1775.
(44) Velický, M.; Toth, P. S.; Rakowski, A. M.; Rooney, A. P.; Kozikov, A.; Woods, C. R.; Mishchenko, A.; Fumagalli, L.; Yin, J.; Zólyomi, V.; Georgiou, T.; Haigh, S. J.; Novoselov, K. S.; Dryfe, R. A. W. Exfoliation of Natural van der Waals Heterostructures to a Single Unit Cell Thickness. *Nat. Commun.* **2017**, *8*, 14410.
(45) Xiong, G.; Meng, C.; Reifenberger, R. G.; Irazoqui, P. P.; Fisher, T. S. A Review of Graphene-Based Electrochemical Micro-supercapacitors. *Electroanalysis* **2014**, *26*, 30−51.
(46) Khoshkbarchi, M. K.; Vera, J. H. Measurement and Correlation of Ion Activity in Aqueous Single Electrolyte Solutions. *AIChE J.* **1996**, *42*, 249−258.

DOI: 10.1021/acsnano.8b06101
ACS Nano 2018, 12, 10463−10472